Small Fishing Vessel Detection Using Polarimetric Observables Fusion with Dual-Polarization Sentinel-1 SAR Data

Dae-Woon Shin (https://orcid.org/0000-0001-6603-2337), Chan-Su Yang (https://orcid.org/0000-0002-6882-7325), *Senior Member, IEEE,* and Armando Marino (https://orcid.org/0000-0002-4531-3102), *Senior Member, IEEE*

***Abstract*—Synthetic Aperture Radar (SAR) is an efficient tool for monitoring ships. However, the detection accuracy of small fishing vessels is insufficient due to radar characteristics and image quality. Therefore, this study proposes a polarimetric fusion method focused on enhancing the detection performance of small fishing vessels using Sentinel-1 Single Look Complex (SLC) images. A combination of VH and VV polarization channels (fusVH) was applied to minimize radio frequency interference and azimuth smearing in SAR for detecting merchant ships, and the reflection symmetry (sym) was generated exploiting the fusVH image. Afterward, when the difference between sym and fusVH was less than 7.2 (dB) and sym was greater than -18.03 (dB), the maximum values of sym and fusVH were used to enhance the pixels of potential small ships. Using both sym and fusVH, small fishing vessels can be separated from merchant ships, which can be easily detected using fusVH images. The results were validated using 14 scenes from 2021 to 2023, and the average matching results were calculated to be 0.84 for the probability of detection rate and 0.29 for the false alarm rate.**

***Index Terms*—polarimetric fusion, small fishing vessel, Sentinel-1, ship detection, reflection symmetry.**

I. Introduction

MARITIME Domain Awareness (MDA) is essential to ensure maritime security due to the threat of illegally operating ships, illegal fishing activity, and maritime accidents [1]. To enhance MDA, several data can be utilized, and among them, Synthetic Aperture Radar (SAR) systems have been widely employed, which provide weather-independent ocean surface data with extensive coverage of marine regions. Radar pulses emitted by SAR satellites predominantly interact with the sea surface through single-bounce surface scattering, whereas objects like ships generally produce double- and multiple-bounce scattering due to their complex superstructure and reflective surfaces [1]-[2]. Consequently, the backscattering intensity of ships is expected to be significantly stronger than the surrounding environment, facilitating the detection of ships using various approaches. However, several factors, such as characteristics of ships, environmental conditions, radar characteristics, image quality, and spatial resolution, influence the effectiveness of SAR-based ship detection. Furthermore, the relative effectiveness of RADARSAT-1 beam modes and ERS-1/2 imagery of ship detection is analyzed, and the outcome depicted that the detection performance is enhanced with decreasing wind speed, increasing incidence angles, and image resolution [3]. However, small ships with dimensions below the spatial resolution of the satellite image remained challenging to detect.

In recent decades, many ship detection approaches have been proposed. Among these approaches, the Constant False Alarm Rate (CFAR) technique has become widely employed to detect ships since ships typically exhibit relatively strong backscattering compared to background sea clutter. In particular, cell averaging CFAR (CA-CFAR) is a simple technique exploiting an assumption that the distribution of the clutter is Gaussian and uses boxcar filtering for detection [4]. Advances to this have been developed, especially with the advent of multi-satellite platforms offering diverse resolutions [5]. Image enhancement methods with feature extraction and combined CFAR were proposed to achieve high ship detection performance [6]. A new CFAR-based detector operating in complex maritime environments is proposed, which utilizes Clutter Intensity Statistics (CIS) for adaptive threshold estimation [7]. Despite these approaches, detecting small ships remains a significant challenge because of their lower backscattering values [8].

In addition to traditional methods, advancements in machine learning, particularly Convolutional Neural Networks (CNNs), have brought new possibilities to ship detection [9]. Researchers have successfully adapted advanced CNN-based models, such as Region-Based CNN (R-CNN), Single Shot MultiBox Detector (SSDD), and You Only Look Once (YOLO), to satellite imagery for experimental ship detection [10]-[12]. Large-scale datasets, such as ship chip images collected from long-term satellite observations, have been

Manuscript received 27 June 2025; revised 2 October 2025; accepted 13 October 2025. This research was supported by the Ministry of Trade, Industry, and Energy under the project "Regional Innovation Cluster Development Program (R&D) (P0025425)" managed by the Korea Institute for Advancement of Technology (KIAT), and the Ministry of Foreign Affairs (IUU Project), Republic of Korea. (Corresponding author: Chan-Su Yang)

Dae-Woon Shin is with the Sea Power Reinforcement and Security Research Department, Korea Institute of Ocean Science & Technology, Busan 49111, Republic of Korea (e-mail: sin6535@kiost.ac.kr).

Chan-Su Yang is with Korea Institute of Ocean Science & Technology, the Ocean Science and Technology School, Korea Maritime & Ocean University, Busan 49112, and University of Science & Technology, Daejeon 34113, Republic of Korea (e-mail: yangcs@kiost.ac.kr).

Armando Marino is with Department of Biological and Environmental Sciences, University of Stirling, Stirling FK9 4LA, UK (e-mail: armando.marino@stir.ac.uk).

compiled to support these models. These datasets and open-source tools like xView3-SAR Deep Learning (DL) models have significantly facilitated training and inference processes for ship detection [13]-[15]. Established datasets have been utilized to refine the networks of DL models such as SAR-ShipNet and YOLOX, leading to improved performance in SAR-based ship detection [16]-[17]. Recent DL based real-time ship detection technologies have demonstrated gradual improvements in both detection accuracy and processing speed [18]. In addition, model development has been undertaken to specifically tailor the approach for small and medium-sized ships [19]. However, recent DL models encounter limitations in detecting small ships due to their minimal representation in SAR images, often covering only a few pixels. This insufficient pixel coverage leads to a lack of distinctive image features, significantly reducing the model's effectiveness.

On the other hand, SAR-based ship detection confronts challenges from Radio Frequency Interference (RFI) and azimuth ambiguities/smearing. Ambiguities occur due to high backscattering from man-made structures. At the same time, RFI is caused by human activities, such as mobile communication systems and other satellites, which might result in false detections [20]-[21]. Azimuth smearing arises from movements of the focused target, which introduces mismatches between the expected and observed doppler of the target, consequently smearing the energy of the target over a larger area and reducing the peak energy, which negatively affects detection accuracy [22]-[24]. Therefore, a method for suppressing RFI and azimuth smearing by combining co- and cross-polarized images from dual-polarized Sentinel-1 GRD data is proposed [25]. However, its performance in detecting small ships remains limited, as the study primarily focused on Automatic Identification System (AIS)-equipped vessels.

Different targets typically interact with differently polarized plane waves in distinct ways, providing characteristic information in terms of amplitude and phase from Polarimetric SAR (PolSAR), and based on this, several detectors have been developed for detecting ships. The polarimetric reflection symmetry detector is based on the principle that the natural environment is expected to have reflection symmetry. In contrast, complex scatterers like ships do not have reflection symmetry [26]-[27]. The detector is applied to the cross-correlation between the co- and cross-polarization channels. The geometrical perturbation Polarimetric Notch Filter (PNF) approach focuses on ships' second-order polarimetric feature vector, which lies in the complement orthogonal space relative to the sea [28]-[30]. The Polarimetric Match Filter (PMF) enhances the contrast between the covariance matrices of sea clutter and ships by considering different scattering mechanisms. Similarly, the Polarimetric Whitening Filter (PWF) and Optimal Polarimetric Detector (OPD) were developed to minimize speckles, and they can be adapted to work in the sea environment [31]-[32]. Sub-look detectors emphasize evaluating the correlation between portions of the image spectrum from single-look SAR data. This is because the spectrum of ships is correlated while the ocean is expected to be uncorrelated [21], [33]. The polarimetric entropy detector considers the randomness of the scattering mechanisms forming the target and assumes the sea is rather polarized, always being a surface. The Entropy is particularly effective at low incident angles [34]-[35]. The Dual-pol Ratio Anomaly Detector (DpolRAD) supports incoherent dual-polarization SAR data, such as Sentinel-1. It is designed for detecting icebergs by monitoring anomalies in volume scattering when surrounded by surface scattering [36]. A context aggregation network is proposed for polarimetric SAR ship detection, leveraging ship-specific scattering characteristics to enhance sea clutter separation [37].

Most existing polarimetric SAR research has primarily focused on data from satellite platforms that provide quad-polarization. In contrast, Sentinel-1, which operates with dual-polarization, has yet to be thoroughly developed for polarimetric SAR applications. Additionally, most prior studies have concentrated on merchant vessels equipped with AIS, with relatively few qualitative studies addressing small-ship detection. To address this gap, recent research has explored small ship detection using Sentinel-1 data, specifically targeting recreational boats, by applying mathematical morphology operators and thresholding approaches [38]. Furthermore, studies have investigated non-metallic inflatable rubber vessels for experimental purposes, utilizing dual-polarimetric Sentinel-1 data [39]. However, these studies are constrained by their emphasis on experiments conducted in inland waters, confining their applicability to open sea environments.

Therefore, this study proposed a polarimetric combination method utilizing Sentinel-1 Single Look Complex (SLC) data to improve the detection of small fishing vessels. The detection target was specified to be small fishing vessels less than 30 meters in length with a Small Fishing Vessel Tracking System (V-Pass) equipped.

Our contributions include the following:

1) The input data for the method consists of VH and VV polarization channels, along with the reflection symmetry detector (sym), derived from the cross-correlation between the co- and cross-polarization channels. A new image customized for small fishing vessels was created through a combination of two polarization channels and sym based on adaptive threshold values, and these values were determined by analyzing many small fishing vessel datasets.
2) The performance was verified by comparing previous ship detectors using long-term satellite images.

The remaining sections of this article are organized as follows. Section II describes the research area and the dataset used in this study. Section III details the proposed method and presents its effectiveness through the small fishing vessel detection case study. Section IV-A performs test application results on representative images and summarizes the results by applying our method and comparing it with other ship detectors over long-term datasets in section IV-B. In section

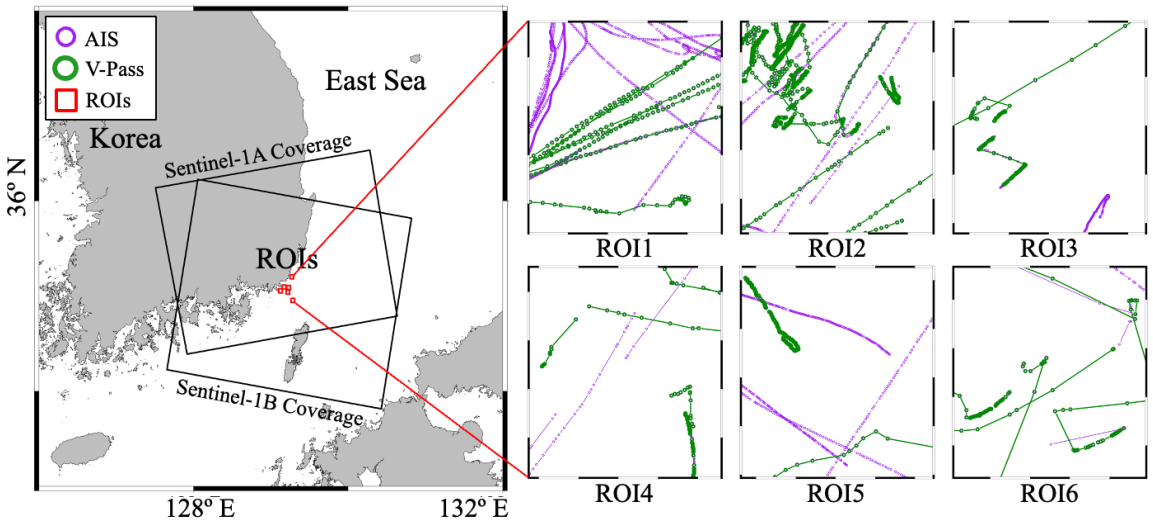

Fig. 1. Study area. (Left) Boundary of Sentinel−1 A and B images (black rectangle). (Right) 6 ROIs and ship trajectories from AIS (Automatic Identification System) and V−Pass (small fishing vessel tracking system). The trajectories represent routes before and after 30 min of the Sentinel−1 image's sensing start time (2021.06.28 21:24:06 UTC).

TABLE I
LIST OF SENTINEL-1 IMAGES USED IN THIS STUDY WITH THE TOTAL NUMBER OF SHIPS OBSERVED BY V-PASS AT EACH DATA ACQUISITION IN 6 ROIS

Scene no.	Satellite	Sensing start time	V-Pass ships
1	S1B	2021.02.28 21:24:01	12
2	S1B	2021.03.24 21:24:01	10
3	S1B	2021.05.23 21:24:04	28
4	S1B	2021.06.28 21:24:06	19
5	S1B	2021.08.03 21:24:08	10
6	S1B	2021.10.02 21:24:02	15
7	S1B	2021.10.14 21:24:11	16
8	S1B	2021.12.13 21:24:09	15
9	S1A	2022.01.12 09:23:20	14
10	S1A	2022.03.13 09:23:19	13
11	S1A	2022.12.26 09:23:27	13
12	S1A	2023.05.31 09:23:28	24
13	S1A	2023.06.12 09:23:28	24
14	S1A	2023.06.24 09:23:29	19
15	S1A	2024.08.17 09:23:34	1

IV-C, the demonstration was performed. Section V includes a discussion of the results and future works, and section VI presents the conclusion of this work.

II. MATERIALS

AIS and V-Pass are being operated by the Korea Institute of Ocean Science and Technology (KIOST) in real time for research purposes [40]-[41]. In addition, Sentinel-1 SAR data are publicly available on the Copernicus website at the study location near Busan port (https://scihub.copernicus.eu/, accessed on 3 March 2023) [42]. V-Pass was developed by the Korea Coast Guard (KCG) to monitor fishing vessels, and it is a reliable source of ground truth for small fishing vessels [43]. In this study, 6 regions of interest (ROI) near Busan Port were considered to observe small fishing vessels (Fig. 1) and compare the detection performance of different algorithms in both Sentinel-1 A and B images.

All Sentinel−1 images of Busan from 28 February 2021 to 17 August 2024 were included in the dataset for ship detection. During the period, only images in which fishing vessels were sufficiently observed were selected, the total number of Sentinel−1 images was confirmed to be 15, as depicted in Table I. Additionally, the fishing vessel information reported by V−Pass at each acquisition time was used as a ground truth dataset. However, some small fishing vessels are difficult to identify in SAR images due to their characteristic [44]. Thus, we used only the ships that could be visually identified in the image for validation.

III. METHODOLOGY

The proposed method considers Sentinel-1 SLC as input data and comprises of two steps: polarimetric combination and ship detection (Fig. 2). The amplitude of a SAR image is a complex number, and from this we can extract $\langle|S_{VH}|^2\rangle$ and $\langle|S_{VV}|^2\rangle$, which represent the intensity of each polarization channel. $\langle S_{VV}S_{VH}^*\rangle$ represents the cross-correlation of the two polarization channels. The latter is also referred to as symmetry detector (sym). To suppress smearing/ambiguities, a combination method is considered that fuses VH and VV in a final image (fusVH). The pixels of fusVH are synthesized as below [25].

a) VH intensity in dB is used or

b) The value 6.53 (dB) subtracted to VV_{dB} is used if the difference between VV_{dB} and VH_{dB} is less than 6.53 (dB):

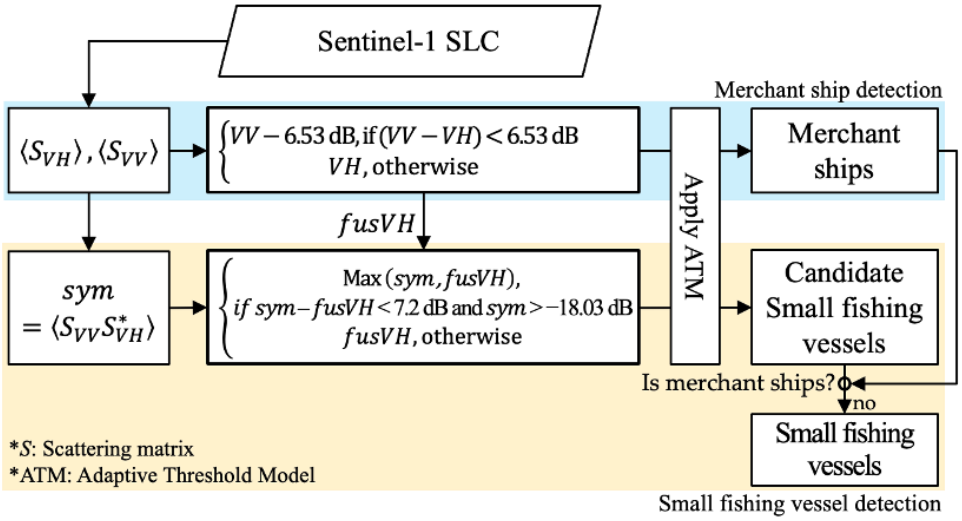

Fig. 2. Overall workflow for small fishing vessels detection using polarimetric combination methods. fusVH is a combined image of VV and VH channels for merchant ship detection.

$$VV_{dB}\text{-}6.53\ (\text{dB}),\ \text{if}\ (VV_{dB}\text{-}VH_{dB}) < 6.53\ (\text{dB}). \quad (1)$$

In the second stage, candidate small fishing vessels are selected using a fusion of two images consisting of sym and fusVH. We call this image fusSym, which is equal to:

a) fusVH is used or

b) Max value of sym and fusVH is used if the difference between sym and fusVH is less than 7.2 (dB) and sym is higher than -18.03 (dB):

$$\text{Max}\ (sym,\ fusVH),\ \text{if}\ sym\text{–}fusVH < 7.2\ (\text{dB}) \quad \text{and}\ \ sym > \text{-}18.03\ (\text{dB}). \quad (2)$$

The thresholds were determined manually by looking at histograms obtained using our long time series of dataset. For ship detection, we classify the merchant ship and small fishing vessel, and Adaptive Threshold Model (ATM) are applied for each image (fusVH, fusSym) based on the target type. Final small fishing vessels are confirmed by separating merchant ships from candidate small fishing vessels. In other words, if the candidate small fishing vessels A is already included in the list of what classified as merchant ships, that candidate A is excluded to the list of fishing vessels and kept as a merchant vessel.

A. Pre-processing

A preprocessing step to obtain input data VV and VH polarization channels was performed with the Sentinel Application Platform (SNAP) software (version 9.0). First, Sentinel−1 SLC images were downloaded from the Copernicus website, and TOPSAR split, radiometric calibration, TopSAR deburst, scattering matrix, multilook, and ellipsoid correction functions were performed in order. Then, a covariance matrix is formed, and the diagonal element |C12| is used for the reflection symmetry detector sym. To utilize the high resolution in the range ground direction provided by SLC, the multilook option was set to 1 x 1 (AZ x RG) (which means no multilook is performed), and the interpolation size in the ellipsoid correction was set to 6 m x 6 m, so that the final pixel spacing size is set to 6 m in width and height.

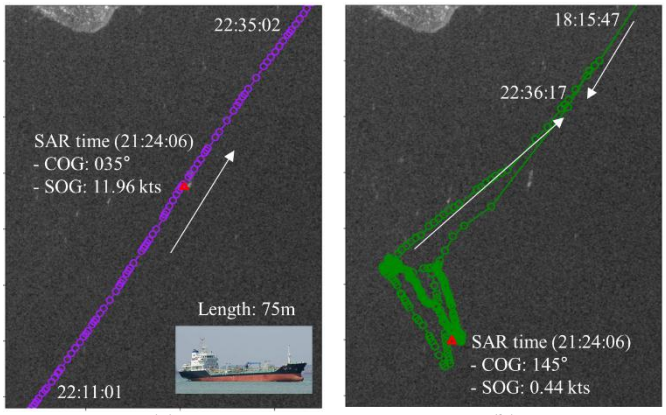

Fig. 3. Ship trajectories used in the case studies. Purple and green circles present the trajectories of (a) a tanker ship from AIS and (b) a small fishing vessel based on V-Pass, respectively. Red triangle indicates the position interpolated to SAR acquisition time (2021.06.28 21:24:06 UTC).

B. Polarimetric Fusion

To demonstrate the procedure used to produce the fusVH (i.e. to suppress smearing/ambiguities), we use two case studies of ships as shown in Fig. 3. An example for a merchant ship was located between ROI1 and ROI2. The ship type (tanker), size (75 m), and length (12 m) information were obtained from AIS (Fig. 3(a)). The ship sailed in a northeast direction (035 deg), and its speed was calculated to be 11.96 kts at the interpolated position during the SAR acquisition

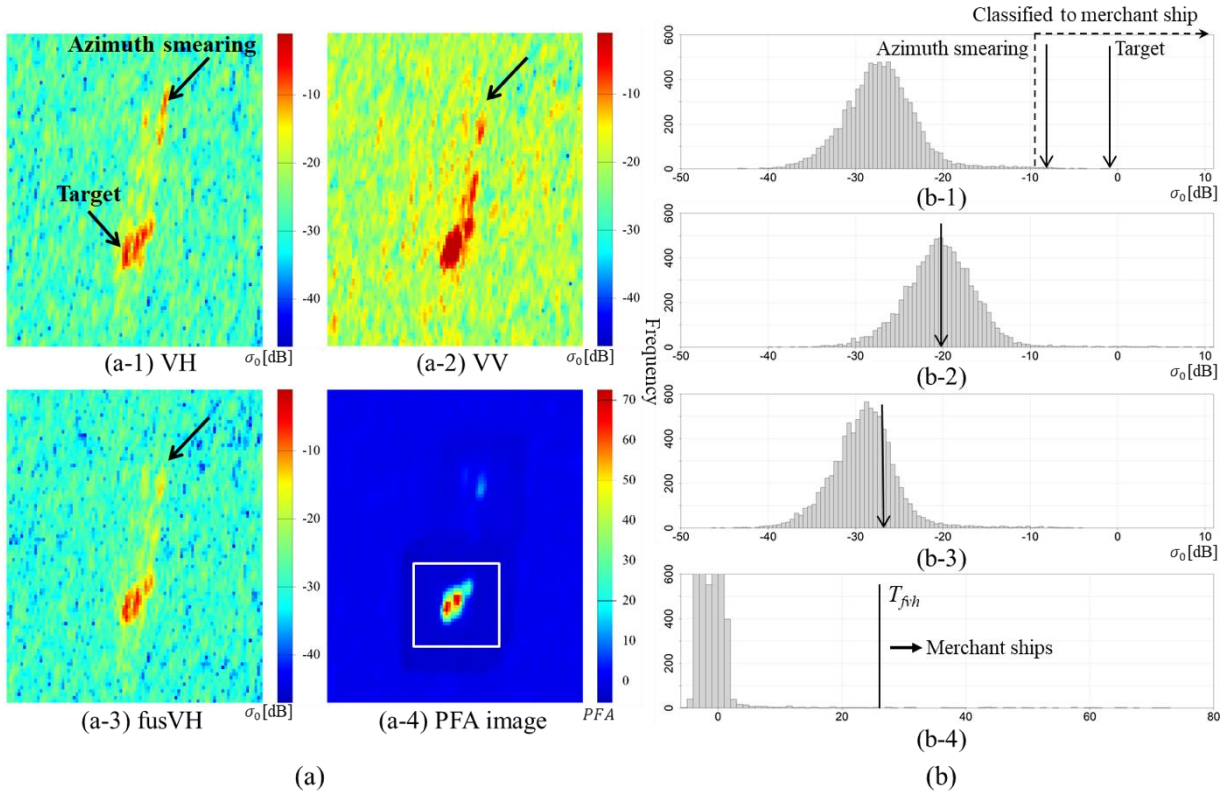

Fig. 4. Visualization of merchant ship detection from the multiple polarization channels. Images from (a-1) to (a-4) display the VH, VV channels, fusVH, and PFA (Probability of False Alarm ratio) image. The image is generated by dividing the value of the background cell from the target cell to display the ATM effect. Histogram (b-1) represents the RCSs of the target and azimuth smearing for the VH. (b-2) shows the RCS at the location where azimuth smearing occurs in VV, and (b-3) represents fusVH. (b-4) indicates the threshold value (T_{fvh}) from the distribution of PFA image to detect the merchant ships. The frequency represents the pixel count for each σ₀ value in the image.

(21:24:06). The trajectory of the small fishing vessel was obtained in ROI2 from V-Pass with samples from 18:15 to 22:36 minutes (Fig. 3(b)). The ship trajectory draws a zig-zag pattern as typical from fishing activity, and interpolated SOG was calculated at less than 1 kts using V-pass data.It is well known that cross-polarization (VH) significantly reduces false detections due to the lower backscattering from waves [45]-[46]. The power at the co-polarization (VV) is considerably greater than the cross-polarization, however it is more affected by azimuth smearing/ambiguities or RFI [20], [22], [23]. Therefore, Bae and Yang [25] proposed a new algorithm to suppress azimuth smearing/ambiguities and RFI by combining the two channels in a fusVH. Fig. 4 shows an example of suppressing smearing/ambiguities using VV, VH, and fusVH. Fig. 4(b-4) also shows the ATM result applied to these images. RCS observed in the area of the tanker ship was -1.19 (dB) in VH (therefore categorized as merchant ship) and shows a high backscattering return in both VV and VH. In Fig. 4(a-1), smearing artifacts were found in the upper (northern) part of the ship in the VH polarization channel. The maximum 4(c-1) shows that the azimuth smearing is successfully removed and converted to a lower RCS of -26.74 (dB) (Fig. 4(a-3), 4(b-3)). For ship detection, a CFAR-based ATM was applied to the generated fusVH image. The parameters of ATM were set to 3 x 3 pixels for the target cell size, 21 x 21, and 31 x 31 for the guard and background cell size. The Probability of False Alarm ratio (PFA) was applied to the threshold value (T_{fvh}) for merchant ship (Fig. 4(b-4)).

The fusVH is effective in removing artifacts such as azimuth smearing/ambiguities. However, it may also suppress the RCS of small fishing vessels. To compensate for these limitations, we used sym. Reflection symmetry is a well-known property of natural targets and is also employed for radar calibration [47]. It states that on some natural targets that do not present orientations other than horizontal or vertical, the co- and cross-polarized channels are uncorrelated [48], [49]. In other words, a sea surface without artificial metallic targets is a composition of randomly distributed scatterers that returns a sym close to 0. On the contrary, sym increases when the target presents orientations [50].

Fig. 5 shows an example of sym to enhance contrast for small fishing vessels. In VH, the maximum RCS in the area of the small fishing vessel was measured as -16.95 (dB) (categorized as a small fishing vessel), which is a considerably low value (Fig. 5(a-1), 5(b-1)). At the same pixel location, VV was measured as -11.92 (dB), which is not a relatively high value compared to the surrounding pixels (Fig. 5(a-2), 5(b-2)). As a result of weak signal for both polarization channels, the

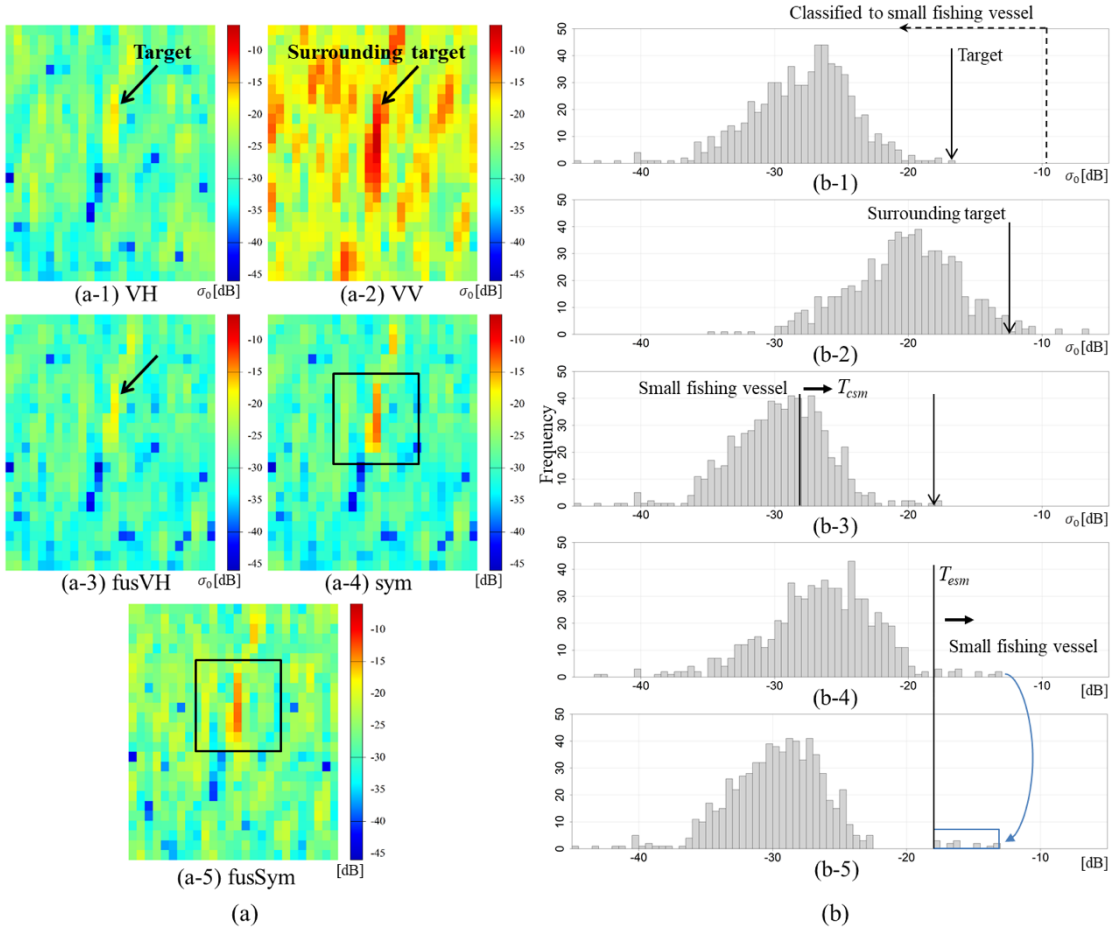

Fig. 5. Illustration of generating fusSym image for small fishing vessel detection. Images from (a-1) to (a-5) display the VH, VV channels, fusVH, sym, and fusSym. Histogram (b-1) shows the RCS of a target for VH, and (b-2) represents the RCS of the surrounding target at the same location in VV. (b-3) indicates the first threshold value (T_{csm}) and RCS suppressed effect from the fusVH. (b-4) represents the second threshold value (T_{esm}) from sym distribution for small fishing vessels, and the value in sym over T_{esm} is used for enhancing RCS in the fusSym (b-5). The frequency represents the pixel count for each σ₀ value in the image.

fusVH (which combines VH and VV) in Fig. 5(a-3), 5(b-3) suppressed the target RCS to -18.45 (dB). In contrast, sym has a value that is higher than the two polarization channels with a maximum RCS of -13.27 (dB) at a small fishing vessel (Fig. 5(a-4), 5(b-4)). In this sample, sym for the small fishing vessel (> -18.03 (dB)) has a higher value than fusVH (-18.45 (dB)). Therefore, the pixels that satisfy the second condition (T_{esm}) in sym are replaced with the one of fusVH (Fig. 5(a-5), 5(b-5)). Additionally, the first condition is also satisfied as shown in Fig. 5(b-3) histogram with higher than T_{csm}. This generated new image is here defined as the fusSym.

In the following, four small fishing vessels were used to check and demonstrate the effectiveness of the proposed method, and a step-by-step process is shown in Fig. 6. These ships were observed in ROI2 from V-Pass, and the RCS for the small fishing vessels ranges between -11.58 and -16.95 (dB) in VH channel. High clutter backscattering in the VH polarization channel can be observed in Fig. 6(a), (b), and (c). Conversely, false targets produced by sea clutter were observed at several locations near the targets in VV. In (d), it is difficult to identify the target in both VH and VV images. Interestingly, the amount of backscattering from the vessel shown by fusVH is reduced, while the small fishing vessel in fusSym presents relatively high backscattering.

The following Peak to Background Contrast ratio (PBC) is computed to examine the detection ability. The PBC was calculated using the target peak of each ship's area defined as $Peak_{Target}$ and the mean value of the surrounding background clutter defined as $Mean_{Background}$ [51]. The target area was 11x11 pixels centered on the ship coordinates, and the background area was set to 26x26 pixels, excluding the target area.

$$PBC_{pol} = \frac{Peak_{Target} - Mean_{Background}}{Peak_{Target} + Mean_{Background}}. \quad (3)$$

A total of 5 ships are shown in Table II, where the results of PBC for each polarization of target1 is in Fig. 5, and target 2~5 is in Fig. 6. Regarding VV and VH, the values of PBC are similar for both channels. Using fusVH does not necessarily

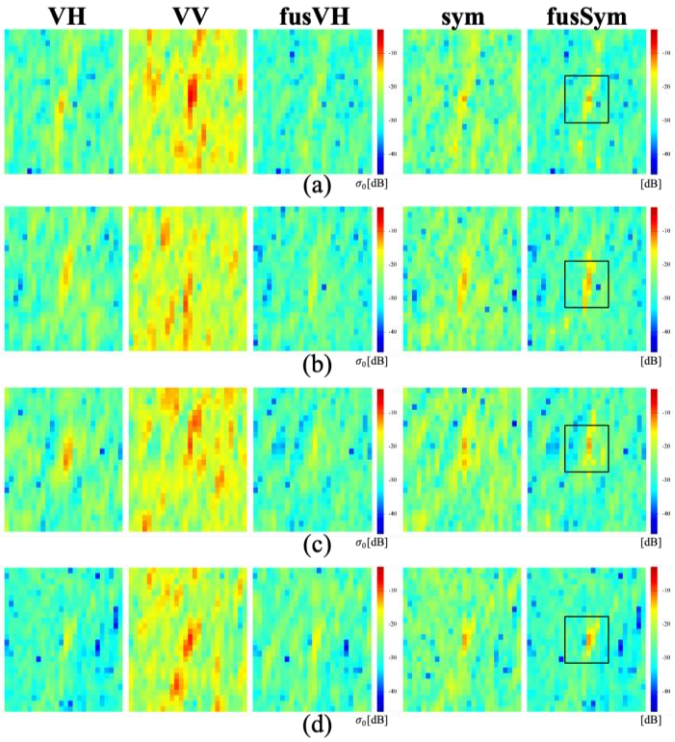

Fig. 6. Application results to four small fishing vessels. VH and VV channels, fusVH, sym, and fusSym images are from left to right, and the black rectangle represents the enhanced area.

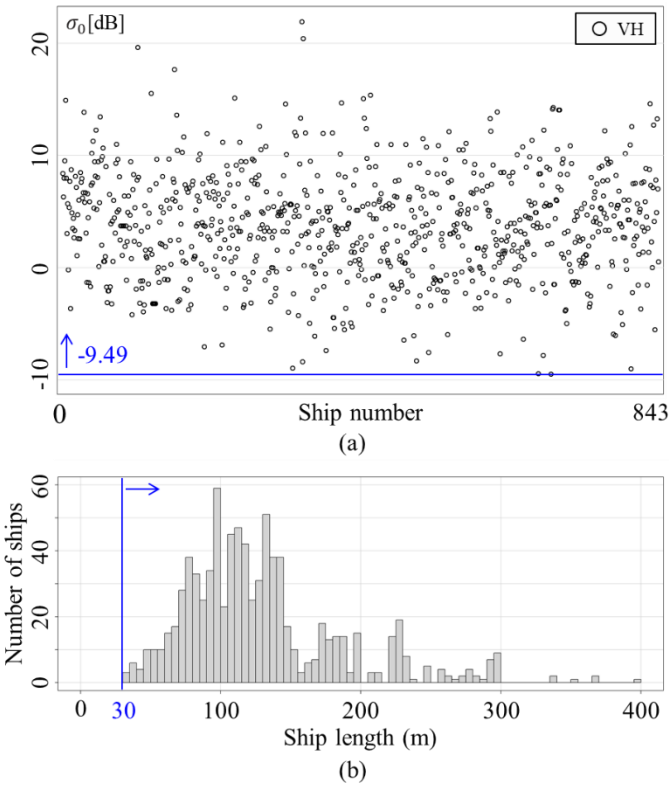

Fig. 7. RCS and ship length distribution from AIS. The datasets are collected from 5 January to 13 December 2021. (a) displays the RCS distribution of 843 ships in the VH polarization channel and minimum RCS (blue line). (b) represents ship length distribution and minimum length (blue line).

TABLE II
PERFORMANCE EVALUATION USING PBC FOR 5 TARGETS. NO. 1 IS THE TARGET USED FOR A CASE STUDY, AND NO. 2 TO 5 IN FIG. 6 ARE TARGETS FOR APPLICATION ADDITIONALLY

no.	Max_{VV}	Max_{VH}	PBC_{VV}	PBC_{VH}	PBC_{fusVH}	PBC_{sym}	PBC_{fusSym}
1	-6.787	-16.951	0.888	0.811	0.858	0.884	0.942
2	-6.292	-13.066	0.874	0.893	0.749	0.861	0.927
3	-9.712	-13.749	0.665	0.869	0.779	0.851	0.923
4	-9.356	-11.577	0.759	0.913	0.851	0.855	0.927
5	-8.266	-16.335	0.846	0.802	0.872	0.884	0.948

improve PBC, while using fusSym shows an improvement in all targets. The PBCs increased from 1% to 7% compared to VH, VV, and sym. The best performance showed a PBC of 0.94 for the five small fishing vessels.

C. Ship Detection

Ship detection is performed in two steps: categorizing RCS and applying thresholds. Different thresholds were applied for each step since the detection targets are classified into merchant and small fishing vessels. To determine the threshold for the first step, the RCS (VH polarization channel) of 843 merchant ships from 18 Sentinel-1 images in 2021 was investigated, as shown in Fig. 7(a). As a result, the minimum RCS was found to be -9.49 (dB), which was used as the threshold to classify and separate merchant ships from small fishing vessels. The second step used adaptive CFAR for merchant ships and small fishing vessels. The parameters of PFA were set to 26 for the fusVH (merchant ship) image and 11 for the fusSym (small fishing vessel) image. Fig. 7(b) illustrates the ship length distribution of 843 AIS ships. The ship length ranges from 30 meters to 400 meters, and this study specifically targeted the detection of small fishing vessels under 30 meters, which are not classified as merchant ships.

The V-Pass was used as ground truth to confirm the presence of small ships. Prior to matching, Dead Reckoning (DR) position interpolation was performed to increase the position accuracy from V-Pass data [52]-[53]. Additionally, the ship position was corrected one more time by calculating the azimuth shifting distance caused by the doppler effect in SAR [54]. A successful matching was called when the distance between the detected location and the ground truth was less than 100 meters.

D. Threshold Determination using Ship Dataset

To determine the parameters for equation (1), a total of 20 Sentinel-1A and Sentinel-1B images were analyzed. They were acquired between 28 December 2017 and 17 December 2018 nearby Busan Port. The VH channel was primarily used do benchmark and find parameters. First, the condition if $(VV_{dB} - VH_{dB}) < 6.53$ (dB) was used to determine the presence

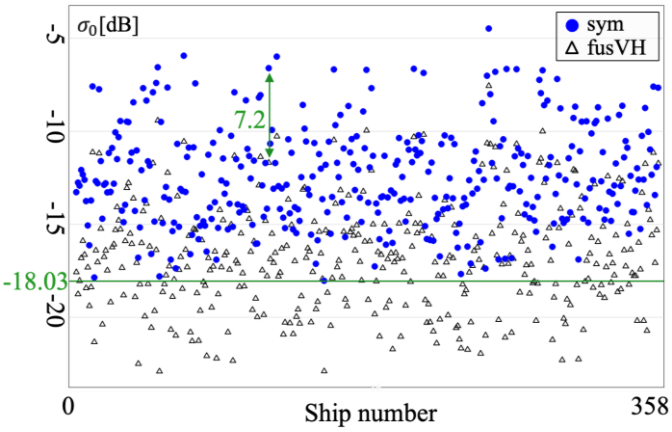

Fig. 8. RCS distribution of 358 fishing vessels in the sym and fusVH image. The datasets are obtained by V-Pass from 5 January to 13 December 2021.

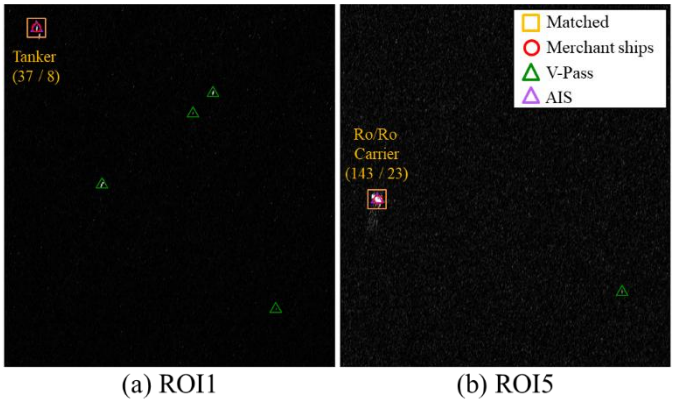

Fig. 9. Detection results for merchant ships in (a) ROI1 and (b) ROI5 (scene no.4). The Red circle indicates the detected position, a green triangle for V-Pass, the purple triangle for AIS represents the ground truth, and the orange rectangle displays the matching results.

of RFI and azimuth smearing. The parameter 6.53 (dB) was selected looking at the histogram and it represents the maximum difference between VV and VH values that can be observed under RFI and azimuth smearing conditions. When the condition is satisfied, VH channel value is replaced by $VV_{dB} - 6.53$ (dB) [25].

To select the parameters for equation (2), we performed a statistical investigation of fishing vessels in a dataset of Sentinel-1 images from 5 January to 13 December 2021 (Fig. 8). The fusVH image was used as the benchmark image. In this stage, using V-Pass to validate our selections, a pixel was considered a candidate small fishing vessel only if it simultaneously satisfied the two conditions: $sym - fusVH < 7.2$ (dB) and $sym > -18.03$ (dB). Both parameters (7.2 (dB) and −18.03 (dB)) were determined through the statistical analysis of a dataset containing 358 small fishing vessels. These parameters were designed to detect the majority of small fishing vessels operating in the study area, with 7.2 (dB) representing the maximum and −18.03 (dB) the minimum observed values for validate fishing vessels in this dataset. If both conditions were satisfied, the corresponding fusVH pixel value was replaced with Max (*sym*, *fusVH*).

IV. Results

In this section, we presented the results applying the proposed method to 15 Sentinel-1 images acquired from 28 February 2021 to 24 August 2024. POD (Probability of Detection) is the ratio of the number of correctly detected ships over the total number of ships present, and it represents the detection accuracy. FAR (False Alarm Rate) is the ratio of unmatched ships to the total number of ship detections [55]-[56]. The closer POD is to 1, the closer FAR is to 0, the better performance.

A. Test Result

The merchant ship detection results obtained from ROI1 and ROI5 are displayed in Fig. 9. In ROI1 (Fig. 9(a)), four small fishing vessels and one merchant ship were observed. The ship was a tanker with a length of 37 m and a width of 8 m. In ROI2 (Fig. 9(b)), two small fishing vessels and one merchant ship were found with a Ro-Ro/Container carrier of length 143 m and width 23 m. Fig. 9 shows that the method using fusVH image successfully detected only the merchant ships.

Fig. 10 displays the small fishing vessel detection results and matches with ground truth. POD was 1 in all ROIs, detecting all 19 small fishing vessels. FAR was calculated as 0 (0/4), 0 (0/5), 0 (0/3), 0 (0/2), 0.5 (1/2), and 0 (0/4) respectively from ROI1 to ROI6. The overall performance of scene no.4 was calculated as an average of 1 for POD and 0.08 for FAR from 6 ROIs. The false detection in ROI5 did not have a matching V-Pass signal; however, after a visual inspection of the image, we observed a strong anomaly in the backscattering. Therefore, we cannot exclude that this was a dark ship with its GPS turned off.

PolSAR has been demonstrated to be very useful in identifying targets at sea. In this work, as a comparison, we tested PMF, PWF, IDPolRAD, PNF, and co- and cross-polarization sub-look detectors (Sub-copol, Sub-crpol). In POD, most detectors show relatively lower performance for small fishing vessels. The fusSym presents the best detection performance with all ship detectors. PNF detector showed the second highest performance (0.64) but still missing some small fishing vessel targets (Fig. 11). Additionally, fusSym achieved the lowest FAR with 0.08, which showed balanced detection performance in both POD and FAR. PNF, again, is the second best, with 0.21.

B. Time Series Analysis

In this section, performance evaluation for POD and FAR was conducted using a long time series of 14 images. From the results of each image, the proposed detector achieved the highest POD and the lowest FAR across all scenes without any omissions (Table III, Table IV). The second-best performance in individual images varied depending on the characteristics of

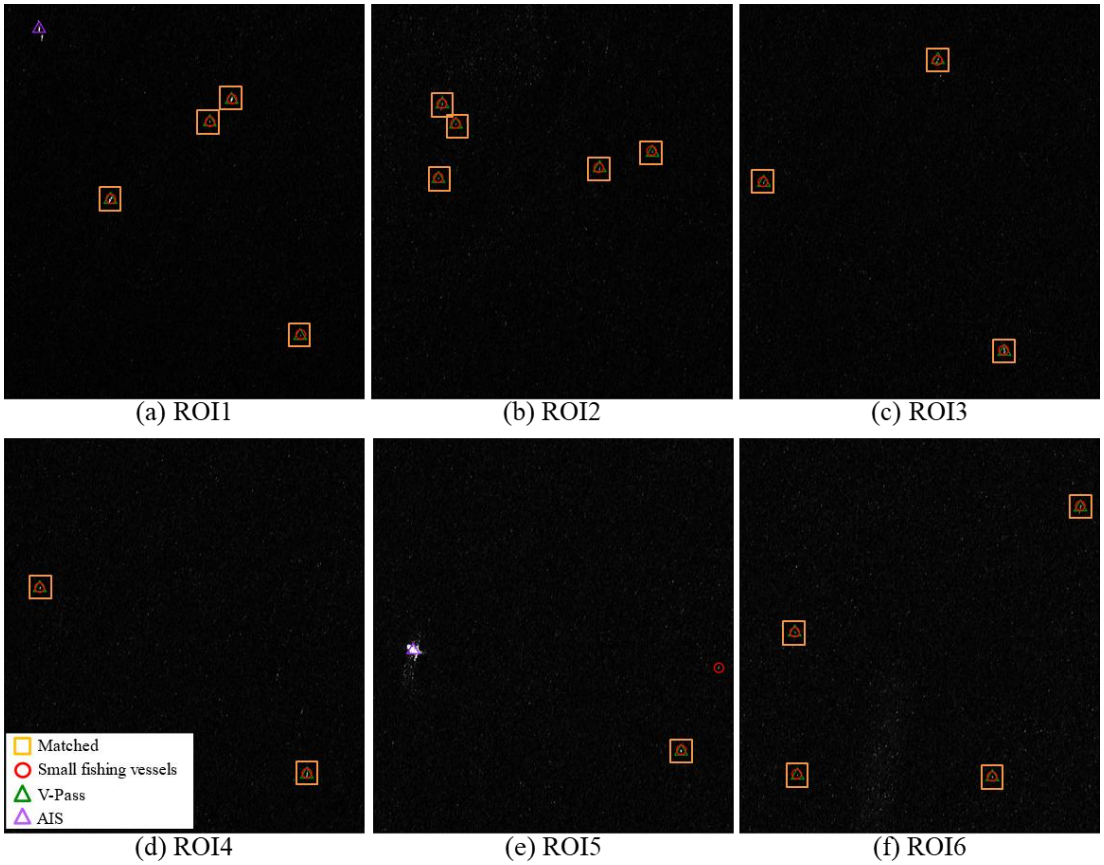

Fig. 10. Detection results for small fishing vessels from (a) ROI1 to (e) ROI6 (scene no.4). The Red circle indicates the detected position, a green triangle for V-Pass, the purple triangle for AIS represents the ground truth, and the orange rectangle displays the matching results.

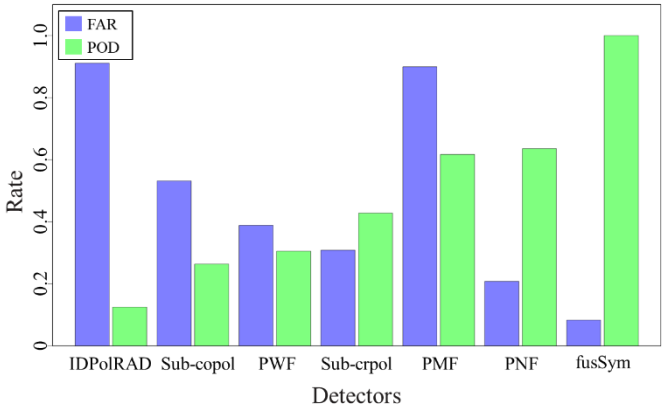

Fig. 11. Comparison graph of ship detectors in scene no.4: POD (Probability of Detection) and FAR (False Alarm Rate).

the scene. Furthermore, for the entire dataset, the detector achieved an average POD of 0.84 and FAR of 0.29. Consequently, the proposed detector showed both a high detection performance and low false compared to other detectors.

C. Final Demonstration using a 10 m Small Fishing Vessel

As a final demonstration, we want to show an example of a small vessel using a Sentinel-1 SAR image acquired at 18:23:14 KST on 17th August 2024 (scene no.15). A small fishing boat was identified as operating in the waters near Jungri port in Yeongdo, and with ship name Ssangdiho (id:36115100), length was measured to be about 10 m, and width was 2.6 m (Fig. 12(b-2,3)). In addition, an on-site observation was performed using a drone to obtain images of the boat drifting at the satellite acquisition time, as shown in Fig. 12(b-1). Fig. 12(a) shows the detection results in the SAR image and the trajectory of the target fishing vessel between 05:31 and 19:31 (KST). Interestingly, the proposed method can identify the 10 m small fishing vessel.

V. Discussion

In this study, we proposed a method to use dual-pol coherent acquisitions to synthesize a new image suitable for detecting small fishing vessels. Detection performance showed superior results compared to other ship detectors, particularly achieving a high detection rate and low false alarm rate. Furthermore, fusVH and sym as intermediate images individually achieved average POD of 0.25 and 0.68, with corresponding FAR of 0.38 and 0.57 across the entire dataset. In contrast, the proposed fusion strategy (0.84, 0.29) clearly demonstrating a significant improvement in detection performance. To visualize and compare the detectors' performance, we illustrate curves using the POD on Y-axis against the FAR. Since detection accuracy was based on ship

TABLE III
COMPARISON TABLE OF SHIP DETECTORS FROM 2021 TO 2023 (14 SCENES): POD (PROBABILITY OF DETECTION)

Scene no.	IDPolRAD	Sub-copol	PWF	Sub-crpol	PMF	PNF	fusSym
1	0.20	0.20	0.37	0.32	0.53	0.65	0.72
2	0.33	0.33	0.72	0.47	0.69	0.78	1.00
3	0.19	0.23	0.35	0.44	0.64	0.59	0.83
4	0.13	0.26	0.31	0.43	0.62	0.64	1.00
5	0.04	0.04	0.36	0.25	0.31	0.28	0.57
6	0.31	0.25	0.44	0.22	0.38	0.29	0.78
7	0.42	0.42	0.67	0.61	0.44	0.67	0.81
8	0.17	0.25	0.39	0.38	0.58	0.51	0.75
9	0.08	0.12	0.00	0.28	0.38	0.63	0.83
10	0.14	0.36	0.19	0.39	0.31	0.58	0.94
11	0.13	0.22	0.26	0.25	0.32	0.35	0.69
12	0.35	0.42	0.32	0.32	0.64	0.42	0.83
13	0.32	0.58	0.32	0.36	0.60	0.87	0.93
14	0.16	0.39	0.14	0.31	0.43	0.47	1.00
Average POD	0.21	0.29	0.35	0.36	0.49	0.55	0.84

TABLE IV
COMPARISON TABLE OF SHIP DETECTORS FROM 2021 TO 2023 (14 SCENES): FAR (FALSE ALARM RATE).

Scene no.	IDPolRAD	Sub-copol	PWF	Sub-crpol	PMF	PNF	fusSym
1	0.79	0.79	0.68	0.60	0.91	0.65	0.39
2	0.88	0.88	0.54	0.56	0.94	0.54	0.17
3	0.69	0.61	0.25	0.25	0.82	0.17	0.08
4	0.91	0.53	0.39	0.31	0.90	0.21	0.08
5	0.98	0.97	0.66	0.78	0.71	0.61	0.40
6	0.63	0.63	0.52	0.67	0.57	0.60	0.31
7	0.65	0.65	0.32	0.49	0.85	0.46	0.17
8	1.00	0.96	0.65	0.55	0.99	0.75	0.30
9	0.98	0.93	1.00	0.80	0.98	0.80	0.58
10	0.98	0.87	0.74	0.81	0.99	0.85	0.44
11	0.97	0.87	0.71	0.74	0.96	0.70	0.45
12	0.99	0.95	0.67	0.52	0.99	0.86	0.33
13	0.75	0.54	0.38	0.58	0.80	0.44	0.09
14	0.92	0.70	0.67	0.65	0.97	0.62	0.29
Average FAR	0.87	0.78	0.58	0.59	0.88	0.59	0.29

position matching, the range of FAR values was not consistent across different detectors. Therefore, FAR were normalized to the range of 0 to 1. Additionally, the Area Under the Curve (AUC) was extracted from the histogram of POD and FAR using different thresholds ranging from 0 to 1 and used to compare detectors quantitatively [39], [55]. The AUC score is evaluated

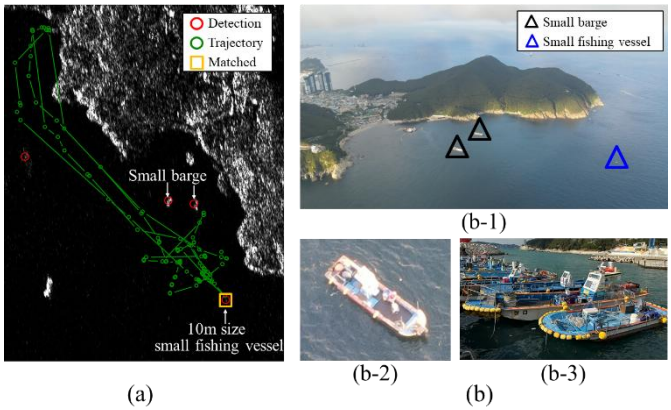

Fig. 12. Field demonstration for 10 m size small fishing vessel detection. (a) Detection results from scene no.15 and vessel trajectory from V-Pass. The red circle indicates the detected position, the green symbol with lines that show the target trajectory, and the orange rectangle displays the matching results. (b-1) Field images from the drone and (b-2,3) enlarged images of the target at sea and port, respectively.

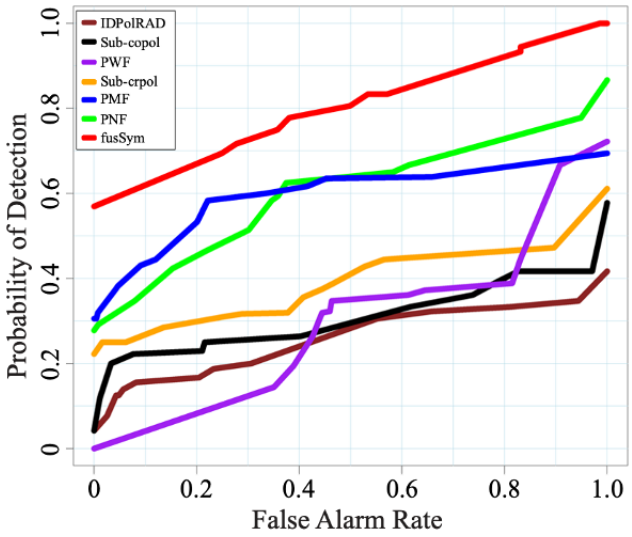

Fig. 13. Plot of Probability of Detection (POD) and False Alarm Ratio (FAR) using different thresholds. FAR is shown in linear scale.

as 0.26 (IDPolRAD), 0.31 (Sub-copol), 0.39 (PWF), 0.29 (Sub-crpol), 0.60 (PMF), 0.60 (PNF), and 0.80 (fusSym), respectively as shown in Fig. 13.

The recent introduction of DL approaches has significantly advanced both the accuracy and processing speed of ship detection algorithms [18]. Nevertheless, notable limitations remain in the detection of small fishing vessels. First, the targets occupy only a few pixels, leading to a high risk of feature loss [57]. Second, scattered speckle noise from sea surface results in a reduced SNR and consequently an increased rate of false detections [15]. Third, most datasets used in previous study are predominantly composed of large vessels, and therefore models for small ships are expected to perform worse [16]-[17]. Two recent studies were compared with the proposed method. These methods were applied to the 6 ROIs of scene no. 4. The detection results showed that LEAD-YOLO (A lightweight, efficient, adaptive design of YOLOv5 for enhanced SAR ship detection)

detected only 2 vessels in VH and no detection in VV among the 19 small fishing vessels [58]. DS-YOLO (Despeckling representation for data-efficient SAR ship detection) detected 3 vessels in VH and 1 vessel in VV [59]. Both models detected two merchant ships in all channels. The evaluation results indicate that detection was confined to large vessels, and the models did not succeed in addressing the challenges of small fishing vessel detection.

A demonstration using a long time series of Sentinel-1 images was successfully conducted to verify the performance of the detection. Finally, we also conducted a real-world experiment with a 10 m length small fishing vessel, demonstrating the capability of the proposed method to detect such small vessels.

As a limitation of this study, visual inspection could not identify small fishing vessels with significantly low backscattering, and therefore, some of these had to be removed from the analysis. To address this, it is necessary to consider using other sensors, such as field observation data. Furthermore, this study was limited to ROIs far from some areas of the coast, where frequent false detections occur due to ambiguities and strong waves. In the future, we will try to develop methods to consider those locations. Another limitation of using Sentinel-1 for small fishing vessels is that the resolution of Sentinel-1 SLC can be up to approximately 22 meters, which limits performance. To enhance the detection performance of small fishing vessels, we want to perform research using high-resolution data ranging from 0.5 meters to 2.5 meters provided by platforms such as Capella and ICEYE.

VI. Conclusions

SAR is an efficient tool for ship detection. However, its detection performance varies depending on ship characteristics, and the detection of small ships has considerable potential for false detection caused by speckle noise or image artifacts.

Thus, we suggested a polarimetric combination-based small fishing vessel detection approach in this study and assessed the results after applying the method to 14 scenes. The study's conclusions are: Two distinct strategies for small fishing vessel detection were implemented by suppressing smearing/ ambiguities and enhancing small fishing vessel RCS from different polarimetric combination methods. For this purpose, a new image fusSym was synthesized using sym with fusVH. The PBC as a performance evaluation of the generated image was increased considerably. The ship detection results were validated using ship data from a small fishing vessel dataset. By utilizing 14 scenes, it was found that the average POD and FAR score for small fishing vessel detection was accomplished at 0.84 and 0.29, respectively. Furthermore, the proposed method showed the highest performance compared with the other 6 detectors on entire scenes. Future research will focus on reducing false detections through evaluations under variable sea state conditions and the development of specialized techniques for coastal regions with severe ambiguities.

References

[1] K. Ouchi, "Current status on vessel detection and classification by synthetic aperture radar for maritime security and safety," *38th Symp. Remote Sens. Enviro. Sci.*, Gamagori, Aichi, Japan, Sep. 3-5, 2016, pp. 5–12.

[2] W. G. Pichel and P. Clemente-Colon, "NOAA coastwatch SAR applications and demonstration," *Johns Hopkins APL Tech. Dig.*, vol. 21, no.1, pp. 49–57, 2000.

[3] P. Vachon and R. Olsen, "RADARSAT: Which mode should I use," *Backscatter.*, vol. 9, pp. 15–20, 1997.

[4] D. J. Crisp, "The state-of-the-art in ship detection in synthetic aperture radar imagery," *DSTO Info. Sci. Lab.*, Edinberg, Australia, Rep. DSTO-RR-0272, May. 2004.

[5] K. El-Darymli, P. McGuire, D. Power, and C. Moloney, "Target detection in synthetic aperture radar imagery: A state-of-the-art survey," *J. Appl. Remote Sens.*, vol. 7, no. 1, May. 2013, Art. no. 071598.

[6] N. Li, X. Pan, L. Yang, Z. Huang, Z. Wu, and G. Zheng, "Adaptive CFAR method for SAR ship detection using intensity and texture feature fusion attention contrast mechanism," *Sensors.*, vol. 22, no. 11, Oct. 2022, Art. no. 8116.

[7] M. Liu, B. Zhu, and H. Ma, "A new synthetic aperture radar ship detector based on clutter intensity statistics in complex environments," *Remote Sens.*, vol. 16, no. 4, Feb. 2024, Art. no. 664.

[8] J. Jeong and C.-S. Yang, "Automatic image contrast enhancement for small ship detection and inspection using RADARSAT-2 synthetic aperture radar data," *Terr. Atmos. Ocean. Sci.*, vol. 27, no. 4, pp. 463–472, Aug. 2016.

[9] A. Shrestha and A. Mahmood, "Review of deep learning algorithms and architectures," *IEEE Access.*, vol.7, pp. 53040-53065, Apr. 2019.

[10] G.-H. Nie, P. Zhang, X. Niu, Y. Dou, and F. Xia, "Ship detection using transfer learned single shot multi box detector," *ITM Web Conf.*, vol. 12, Sep. 2017, Art. no. 01006. doi: https://doi.org/10.1051/itmconf/20171201006.

[11] Y. Gui, X. Li, L. Xue, and J. Lv, "A scale transfer convolution network for small ship detection in SAR images," *in Proc. 2019 IEEE 8th Joint Intl. IT and AI Conf. (ITAIC).*, Chongqing, China, May. 24-26, 2019, doi: https://doi.org/10.1109/ITAIC.2019.8785805.

[12] Y.-L. Chang, A. Anagaw, L. Chang, Y.C. Wang, C.-Y. Hsiao, and W.-H Lee, "Ship detection based on YOLOv2 for SAR imagery," *Remote Sens.*, vol. 11, no. 7, Apr. 2019, Art. no. 786.

[13] T. Zhang et al., "LS-SSDD-v1.0: A deep learning dataset dedicated to small ship detection from large-scale Sentinel-1 SAR images," *Remote Sens.*, vol. 12, no. 18, Sep. 2020, Art. no. 2997.

[14] T. Zhang et al., "SAR Ship Detection Dataset (SSDD): Official release and comprehensive data analysis," *Remote Sens.*, vol. 13, no. 18, Sep. 2021, Art. no. 3690.

[15] F. Paolo et al., "xView3-SAR: Detecting dark fishing activity using synthetic aperture radar imagery," *Adv. Neural Inf. Process. Syst.*, 2022, vol. 35, Nov. 2022. arXiv:2206.00897.

[16] Y. Deng, D. Guan, Y. Chen, W. Yuan, J. Ji, and M. Wei, "SAR-ShipNet: SAR ship detection neural network via bidirectional coordinate attention and multi-resolution feature fusion," *in Proc. Int. Conf. on Acoustics, Speech, and Signal Processing (ICASSP)*, Singapore, May. 22-27, 2022. arXiv:2203.15480.

[17] H. Wang, D. Han, M. Cui, and C. Chen, "NAS-YOLOX: a SAR ship detection using neural architecture search and multi-scale attention," *Connect Sci.*, vol. 35, no. 1, pp. 1–32, Oct. 2023.

[18] J. Li, J. Chen, P. Cheng, Z. Yu, L. Yu, and C. Chi, "A survey on deep-learning-based real-time SAR ship detection," *IEEE J. Sel. Topics Appl. Earth Observ. Remote Sens.*, vol. 16, pp. 3218–3247, Mar. 2023.

[19] T. Guan, S. Chang, C. Wang, and X. Jia, "SAR small ship detection based on enhanced YOLO network," *Remote Sens.*, vol. 17, no. 5, Feb. 2025, Art. no. 839.

[20] F. J. Meyer, J. B. Nicoll, and A. P. Doulgeris, "Correction and characterization of radio frequency interference signatures in L-band synthetic aperture radar data," *IEEE Trans. Geosci. Remote Sens.*, vol. 51, no. 10, pp. 4961–4972, Oct. 2013.

[21] K. Ouchi, S. Tamaki, H. Yaguchi, and M. Iehara, "Ship detection based on coherence images derived from cross correlation of multilook SAR images," *IEEE Geosci. Remote Sens. Lett.*, vol. 1, no. 3, pp. 184–187, Jul. 2004.

[22] J. R. Fienup and A. M. Kowalczyk, "Detecting moving targets in SAR imagery by using a phase-error correction algorithm," *Proc. algorithms for SAR imagery II*. Bellingham, WA, USA, vol. 2487, pp. 337–344, Jun. 1995.

[23] C. A. Liu, "A dual-polarization ship detection algorithm," *Def. Res. Dev.*, Ottawa, Canada, Rep. DRDC-RDDC-2015-R109, Nov. 2015.

[24] J. Song, D.-J. Kim, and K.-M. Kang, "Automated procurement of training data for machine learning algorithm on ship detection using AIS information," *Remote Sens*., vol. 12, no. 9, May. 2020, Art. no. 1443.

[25] J. Bae and C.-S. Yang, "A method to suppress false alarms of Sentinel-1 to improve ship detection," *Korean J. Remote Sens*., vol. 36, no. 4, pp. 535–544, Aug. 2020.

[26] F. Nunziata, M. Migliaccio, and C. E. Brown, "A physically-based approach to observe ships in dual-polarized SAR data," *in Proc. IEEE Intl. Geosci. and Remote Sens. Symp.*, Honolulu, HI, USA, Jul. 2010.

[27] F. Nunziata, M. Migliaccio, and C.E. Brown, "Reflection symmetry for polarimetric observation of man-made metallic targets at sea ocean," *Eng. IEEE J.*, vol. 37, no. 3, pp. 384–394, Jul. 2012.

[28] A. Marino, N. Walker, and I. Woodhouse, "Ship detection using SAR polarimetry. the development of a new algorithm designed to exploit new satellite SAR capabilities for maritime surveillance," *in Proc. SeaSAR.*, Frascati, Italy, vol. 679, Jan. 25-29, 2010, id. 36.

[29] A. Marino and N. Walker, "Ship detection in variable sea states and depolarized sea clutter: a polarimetric notch filter," *PolinSAR 2011 Sci. Appl. SAR Polarim. Polarim. Interfero.*, vol. 695, Mar. 24-28, 2011, id. 32.

[30] G. Gao, and G. Shi, "Ship detection in dual-channel ATI-SAR based on the notch filter," *IEEE Trans. Geosci. Remote Sens.*, vol. 55, no. 8, pp. 4795–4810, Aug. 2017.

[31] L. M. Novak, M. B. Sechtin, and M. C. Burl, "Algorithms for optimal processing of polarimetric radar data," *Massachusetts Inst. Tech. Lexington Lincoln Lab*., Lexington, MA, USA, Rep. ADA217330, Nov. 1989.

[32] J. Yang and Y. A. Cui, "Novel method for ship detection in polarimetric SAR images using gopce," *in Proc. IET Intl. Radar Conf.*, Guilin, China, Apr. 2009.

[33] A. Marino, M. J. Sanjuan-Ferrer, I. Hajnsek, and K. Ouchi, "Ship detection with spectral analysis of synthetic aperture radar: a comparison of new and well-known algorithms," *Remote Sens.*, vol. 7, no. 5, pp. 5416–5439, Apr. 2015.

[34] R. Touzi, F. Charbonneau, R. K. Hawkins, K. Murnaghan, and X. Kavoun, "Ship-sea contrast optimization when using polarimetric SARs," in Proc. IGARSS 2001, Sydney, Australia, vol. 1, Jul. 9-13, 2001. pp. 426–428.

[35] J. Chen, Y. Chen, and J. Yang, "Ship detection using polarization cross-entropy," *IEEE Geosci. Remote Sens.*, vol. 6, no. 4, pp. 723–727, Oct. 2009.

[36] A. Marino, W. Dierking, and C. A. Wesche, "Depolarization ratio anomaly detector to identify icebergs in sea ice using dual-polarization SAR images," *IEEE Trans. Geosci. Remote Sens.*, vol. 54, no. 9, pp. 5602–5615, Sep. 2016.

[37]C. Hu, H. Chen, X. Sun, and F. Ma, "Polarimetric SAR ship detection using context aggregation network enhanced by local and edge component characteristics," *Remote Sens.*, vol. 17, no. 4, Feb. 2025, Art. no. 568.

[38] M. Ruciński, E. Woźniak, S. Kulczyk, and M. Derek, "Small recreational boat detection using Sentinel-1 data for the monitoring of recreational ecosystem services," *Remote Sens.*, vol. 15, no. 7, Mar. 2023, Art. no. 1807.

[39] P. Lanz, A. Marino, T. Brinkhoff, F. Köster, and M. Möller, "The InflateSAR campaign: Testing SAR vessel detection systems for refugee rubber inflatables," *Remote Sens.*, vol. 13, no. 8, Apr. 2021, Art. no. 1487.

[40] T.-H. Kim, J. Jeong, and C.-S. Yang, "Construction and operation of AIS system on Socheongcho ocean research station," *J. Coast. Disaster Prev.*, vol. 3, no. 2, pp. 74–80, Apr. 2016.

[41] J. Jeong, T.-H. Kim, and C.-S. Yang, "Construction of real-time remote ship monitoring system using Ka-band payload of COMS," *Korean J. Remote Sens.*, vol. 32, no. 3, pp. 323–330, Apr. 2016.

[42] D. Štepec, T. Martinčič, and D. Skočaj, "Automated system for ship detection from medium resolution satellite optical imagery," *in Proc. Ocans 2019 MTS/IEEE Seattle*, Seattle, WA, USA, Oct. 2019. doi: https://doi.org/10.23919/OCEANS40490.2019.8962707.

[43] Korea Law Information Center. Fishing Vessel Act, 2020.

[44] L. Huang et al., "OpenSARShip: A dataset dedicated to Sentinel-1 ship interpretation," *IEEE J. Sel. Topics Appl. Earth Observ. Remote Sens.*, vol. 11, no. 1, pp. 195–208, Jan. 2018.

[45] P. W. Vachon and J. Wolfe, "C-band cross-polarization wind speed retrieval," *IEEE Geosci. Remote Sens. Lett.*, vol. 8, no. 3, pp. 456–459, May. 2011.

[46] T. N. A. Hannevik, K. Eldhuset, and R. B. Olsen, "Improving ship detection by using polarimetric decompositions," *Norwegian Def. Res. Estab*., Kjeller, Norway, 2015.

[47] J. V. Zyl, C. Papas, and C. Elachi, "On the optimum polarization of incoherently reflected waves," *IEEE Trans. Antennas Propag.*, vol. 35, no. 7, pp. 818–825, Jul. 1987.

[48] S. H. Yueh, R. Kwok, and S. V. Nghiem, "Polarimetric scattering and emission properties of targets with reflection symmetry," *Radio Sci*., vol. 29, no. 6, pp. 1409–1020, Nov. 1994.

[49] C. E. Baum and H. N. Kritikos, eds., *Electromagnetic Symmetry*. New York: Taylor & Francis, 1995, ch.1 and 2.

[50] S. V. Nghiem, S. H. Yueh, R. Kwok, and F. K. Li, "Symmetry properties in polarimetric remote sensing," *Radio Sci.*, vol. 27, no. 5, pp. 693–711, Sep. 1992.

[51] K. Ouchi, and C.-S. Yang, "Combination of entropy and coherence of HH/VV-polarimetric SAR data to improvement of target detection in the sea," *IEICE Tech Rep.*, vol. 114, Oct. 22-24, 2014, pp. 145-150.

[52] A. Harati-Mokhtari, A. Wall, P. Brooks, and J. Wang, "Automatic Identification System (AIS): Data reliability and human error implications," *J. Navig.*, vol. 60, no. 3, pp. 373–389, Sep. 2007.

[53] S. K. Chaturvedi, C.-S. Yang, K. Ouchi, and P. Shanmugam, "Ship recognition by integration of SAR and AIS," *J. Navig.*, vol. 65, no. 2, pp. 323–337, Apr. 2012.

[54] K. Ouchi, "Principles of synthetic aperture radar for remote sensing," Ph.D. dissertation, Tokyo Denki Univ., Tokyo, Japan, 2009.

[55] D.-W. Shin, C.-S. Yang, S. J. K. Chowdhury, "Enhancement of small ship detection using polarimetric combination from Sentinel−1 imagery," *Remote Sens.*, vol. 16, no. 7, Mar. 2024, Art. no. 1198.

[56] K.-A. Park, J.-J. Park, J.-C. Jang, J.-H. Lee, S. Oh, and M. Lee, "Multi-spectral ship detection using optical, hyperspectral, and microwave SAR remote sensing data in coastal regions," *Sustainability.*, vol. 10, no.11, Nov. 2018, Art. no. 4064.

[57] L. Liu, L. Fu, Y. Zhang, W. Ni, B. Wu, Y. Li, C. Shang, and Q. Shen, "CLFR-Det: Cross-level feature refinement detector for tiny-ship detection in SAR images," *Knowledge-Based Systems*, vol. 284, Art. no. 111284, Dec. 2024.

[58] H. Mo, J. Wu, H. Xia, X. Yu, and E. Zhao, "A lightweight, efficient, adaptive design of YOLOv5 for enhanced SAR ship detection," *Remote Sens. Lett.*, vol. 16, no. 5, pp. 549–559, Mar. 2025.

[59] R. Hu, H. Lin, Z. Lu, and J. Xia, "Despeckling representation for data-efficient SAR ship detection," *IEEE Geosci. Remote Sens. Lett.*, vol. 22, Art. no. 4002005, Jan. 2025.

Dae-Woon Shin received the M.Sc. degree in marine traffic engineering and Ph.D. degree in marine science & convergence engineering from Korea Maritime and Ocean University, Busan, South Korea, in 2016 and 2025, respectively. His research interests include ship and oil spill detection using synthetic aperture radar and ship trajectory management based on artificial intelligence.

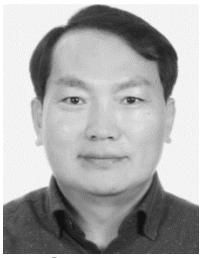

Chan-Su Yang (Senior Member, IEEE) received the Ph.D. degree in coastal application studies of satellite remote sensing from the Department of Civil Engineering from Tohoku University, Sendai, Japan, in 2001. He is a Principal Research Scientist with the Korea Institute of Ocean Science and Technology, Busan, South Korea. He is also a Professor with Korea University of Science & Technology, Daejeon and School of Ocean Science and Technology, KMOU, Busan, South Korea. His research interests include the fields of satellite ocean monitoring and SAR applications.

Armando Marino (Senior Member, IEEE) received the M.Sc. degree in telecommunication engineering from the Universita' di Napoli "Federico II," Naples, Italy, in 2006, and the Ph.D. degree in polarimetric SAR interferometry from the School of Geosciences, University of Edinburgh, Edinburgh, U.K., in 2011. In 2006, he joined the High Frequency and Radar Systems Department, German Aerospace Centre, Oberpfaffenhofen, Germany, where he developed his M.Sc. thesis. From March 2011 to October 2011, he was with the Institute of Computing Research, University of Alicante, Alicante, Spain. From December 2011 to May 2015, he was a Post-Doctoral Researcher and a Lecturer with the Institute of Environmental Engineering, ETH Zürich, Zürich, Switzerland. In June 2015, he was a Lecturer with the School of Engineering and Innovation, Open University, Milton Keynes, U.K. Since May 2018, he has been an Associate Professor at the University of Stirling, Faculty of Natural Sciences, Stirling, U.K.